JFM RAPIDS
journals.cambridge.org/rapids

On the role of adaptivity for robust laminar flow control

Nicolò Fabbiane[1,†], **Bernhard Simon**[2], **Felix Fischer**[2], **Sven Grundmann**[2], **Shervin Bagheri**[1] **and Dan S. Henningson**[1]

[1]Linné FLOW Centre, KTH Mechanics, S-10044 Stockholm, Sweden

[2]Center of Smart Interfaces, TU Darmstadt, Flughafenstraße 19, 64347 Griesheim, Germany

In boundary-layer flows, one may reduce skin-friction drag by delaying the onset of laminar-to-turbulent transition via the attenuation of small-amplitude Tollmien–Schlichting (TS) waves. In this work, we use numerical simulations and experiments to compare the robustness of adaptive and model-based techniques for reducing the growth of two-dimensional TS disturbances. In numerical simulations, the optimal linear quadratic Gaussian (LQG) regulator shows the best performance under the conditions it was designed for. However, it is found that the performance deteriorates linearly with the drift of the Reynolds number from its nominal value. As a result, an order-of-magnitude loss of performance is observed when applying the computation-based LQG controller in wind-tunnel experiments. In contrast, it is shown that the adaptive filtered-X least-mean-squares (FXLMS) algorithm is able to maintain an essentially constant performance for significant deviations of the nominal values of the disturbance amplitude and Reynolds number.

1. Introduction

In recent decades the spatiotemporal behaviour of the instabilities leading to transition from a laminar to a turbulent regime in boundary-layer flows has been thoroughly characterized. In a low-turbulence environment the initial phase of the transition process is an exponential growth of Tollmien–Schlichting (TS) waves (Saric, Reed & Kerschen 2002). Both numerical and laboratory experiments have shown that it is possible to use linear control techniques to damp the amplitude of the instabilities by several orders of magnitude, with the consequences that the

---

† Email address for correspondence: nicolo@mech.kth.se

transition is delayed and the skin-friction drag is reduced (Lundell 2007; Bagheri & Henningson 2011; Goldin *et al.* 2013; Semeraro *et al.* 2013*a*). However, the linear control approach has not yet been established as a competitive technique in applied settings, and essentially all work is at a proof-of-concept level. An understanding of how linear controllers perform under varying conditions is a first step towards making this flow control approach a realistic and competitive alternative in applications.

One of the first attempts to design a compensator in order to delay the laminar-to-turbulent transition was presented by Bewley & Liu (1998). Optimal and robust control theory were used to precompute the compensator based on a state-space formulation of the governing equations. It was a natural extension of the classical Orr–Sommerfeld theory; by connecting the inputs to outputs via a compensator, all aspects of disturbance dynamics – which was previously performed for the open-loop system – could now be performed for the closed-loop system. The optimality and the guaranteed stability of the closed-loop system (under certain conditions, Doyle 1978; Glad & Ljung 2000) resulted in a rapid spread in the stability community (Bagheri, Brandt & Henningson 2009; Barbagallo, Sipp & Schmid 2009; Semeraro *et al.* 2013*b*; Juillet, McKeon & Schmid 2014). In this class of static methods the compensator is first precomputed offline based on a linear model of the flow and then applied to the laboratory or numerical experiment. The most widely used compensator in this context is the linear quadratic Gaussian (LQG) regulator. In contrast, in adaptive control techniques, which were first employed in the work of Sturzebecher & Nitsche (2003), the control law is not precomputed but it is identified online, i.e. the algorithm is able to adjust the compensator through measurements and only partial modelling of the flow response is required. In this category of methods – with the filtered-X least-mean-squares (FXLMS) algorithm being the most common one – the stability of the closed-loop system is not guaranteed and the disturbance energy is not reduced in an optimal way (Aström & Wittenmark 1995).

The aim of this work is to compare the robustness of static and adaptive controllers and assess their advantages and limitations. First, we investigate the robustness of the closed-loop system in experiments by applying an LQG compensator that is designed based on a numerical model of the experimental configuration. This approach has many uncertainties incorporated, since a perfectly exact model of the flow, actuators, sensors and disturbances is not possible to obtain. Second, we compare the performance of LQG and FXLMS by systematically inducing a drift in the Reynolds number and the disturbance amplitude.

2. Experimental set-up

A 2D TS wave is generated by a disturbance source (denoted by d in figure 1) in a flat-plate boundary-layer flow and is detected further downstream by a surface hot wire (y in figure 1). This sensor provides the reference signal to the compensator to compute the control action, and a dielectric barrier discharge (DBD) plasma actuator (u) provides the prescribed forcing on the flow. A second surface hot-wire sensor (z) is positioned downstream of the actuator to evaluate the compensator performance.

The experiments are conducted in an open-circuit wind tunnel at TU Darmstadt, which provides a 450 mm $\times$ 450 mm test section and an averaged turbulence intensity of $Tu = 0.1\%$, measured at the end of the 1:24 contraction nozzle. A 1600 mm long flat plate with a 1:6 elliptical leading edge and an adjustable trailing edge is mounted horizontally in the middle of the test section. Figure 1 shows a sketch of the flat plate containing surface mounted sensors, the disturbance source and the plasma actuator.
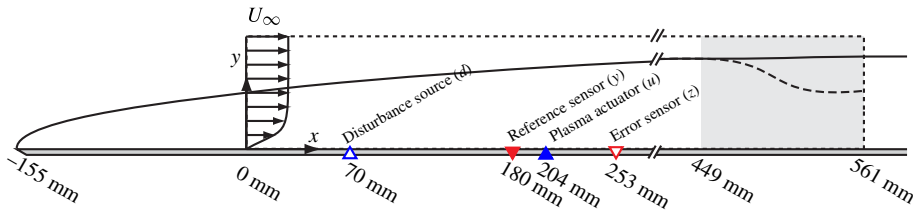
FIGURE 1. Experimental set-up. The computational domain used in the direct numerical simulation (DNS; dashed line) starts at $(x, y) = (0, 0)$ and it extends $750\,\delta_0^*$ in the streamwise direction and $30\,\delta_0^*$ in the wall-normal direction, where $\delta_0^* = 0.748$ mm is the displacement thickness at the beginning of the domain. In the last part of the domain (grey area), a fringe region enforces the periodicity along the streamwise direction (Nordström, Nordin & Henningson 1999).

The zero position is chosen to be 70 mm upstream of the disturbance source as the DNS computational box starts at this point.

A dSPACE system consisting of a DS1006 processor board, a DS2004 A/D board as well as a DS2102 high-resolution D/A board provides the computational power for the flow control algorithm. An additional 16bit NI PCI 6254 A/D board is used for data acquisition of hot-wire sensors signals as well as the disturbance source signals.

Disturbances are created by pressure fluctuations at the wall, caused by conventional loudspeakers. The disturbance source consists of 16 Visaton BF 45 speakers, amplified by 16 Kemo M031N, which can be controlled individually by the 16-channel analogue output module NI9264. The set of loudspeakers is placed outside the test section and 1.2 m long tubes are led into the test section from below the flat plate. The tubes are arranged along a line in the spanwise direction beneath a 0.2 mm wide slot in the surface of the flat plate, while the construction principle is similar to that of Borodulin, Kachanov & Koptsev (2002) and Würz *et al.* (2012). Five tubes with an outer diameter of 3 mm are connected to every loudspeaker, giving a total width of the disturbance source of 240 mm. Two spanwise rows of 30 Sennheiser KE 4-211-2 microphones enable the online monitoring of the phase and amplitude of the artificially excited TS waves in order to assure an even 2D wavefront (figure 2). The first row is positioned upstream of the plasma actuator at $x = 164$ mm while the second row is downstream of the plasma actuator at $x = 224$ mm. All microphones are mounted below the surface and are connected to the surface through a 0.2 mm circular orifice with a spacing of only 9 mm in the spanwise direction. All channels are sampled by two NI 9205 A/D converter modules with 4 kHz.

In addition, a Dantec 55P15 boundary-layer hot-wire probe is mounted on a 2D traverse for phase-averaged boundary-layer measurements. The DC signal is filtered with a 1 kHz low-pass filter to avoid aliasing.

2.1. *Actuator and sensors for flow control*

The plasma actuator consists of a 10 mm wide grounded lower electrode of 35 µm thickness and a 5 mm wide upper electrode, which are divided in the vertical direction by five layers of Kapton tape with a total thickness of 0.3 mm. A GBS Minipuls 2.1 high-voltage supply drives the 230 mm long plasma actuator, which is installed flush mounted to a spanwise groove in order to minimize roughness of the surface.

The plasma actuator driving frequency f_{PA} is chosen to be 10 kHz, which is more than one order of magnitude higher than the unstable TS wave frequency band for this experiment. In order to assure a stable discharge in time and space, an operation range
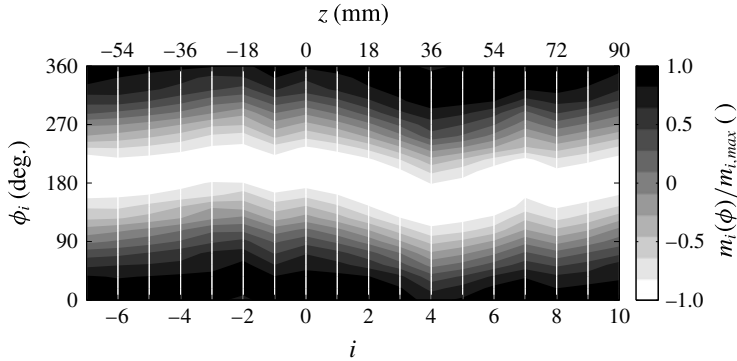
FIGURE 2. Phase-averaged microphone signals $m_i(\phi)$ for a 200 Hz TS wave: the wavefront is aligned along the spanwise direction resulting in a 2D disturbance. The signals are from the upstream microphone row and are sampled at 4 kHz and time averaged for 10 s.

from $V = 5$ kV$_{pp}$ to 13 kV$_{pp}$ has to be maintained for this actuator design (Barckmann 2014); therefore, a mean voltage supply $V = 7$ kV$_{pp}$ is chosen for all experiments. The compensator can modulate the amplitude of the high-voltage supply via the control signal $u(t)$ and, as consequence, vary the plasma actuator force on the time scale of the TS waves. The control signal $u(t)$, fed into the high-voltage generator, is a linearized function with respect to the plasma actuator force at that working point.

Two surface hot-wire sensors are used to provide the compensator with the required information to compute a suitable control signal $u(t)$. As introduced by Sturzebecher & Nitsche (2003), the surface hot wire has proven to be an excellent sensor type for reactive flow control (Lundell 2007; Kurz *et al.* 2013). Due to the high electromagnetic interference of the plasma actuator, a classic hot-wire design with prongs is preferred and is modified to serve as a surface hot wire. Two conventional needles are moulded in a plastic case, which can be flush mounted on the flat plate. A small groove between the needle tips avoids heat loss to the structure and improves the signal-to-noise ratio. The 5 µm thin and 1.25 mm long gilded tungsten wire is heated with an overheat ratio of 1.7. Due to shielded signal lines, this sensor is less sensitive for electromagnetic interferences than the conventional surface hot-wire design based on photo-etched printed circuit boards. A four-channel Dantec Streamline constant-temperature anemometer (CTA) provides the band pass filtered AC signal of the sensors (10 Hz–1 kHz). All hot-wire sensor signals are acquired with a sample rate of 10 kHz. The surface hot wires are calibrated for quantifying the TS wave amplitude according to the definition in (4.1). The calibration is conducted by exciting 2D TS waves whose maximum amplitude is measured above the surface hot wire using the traversable boundary-layer hot-wire probe as a reference.

3. Static and adaptive compensators

Given the sensor measurements, the compensator provides the control sign to the actuator (figure 3). The compensator response is described by the finite-impulse-response (FIR) filter (Haykin 1986),

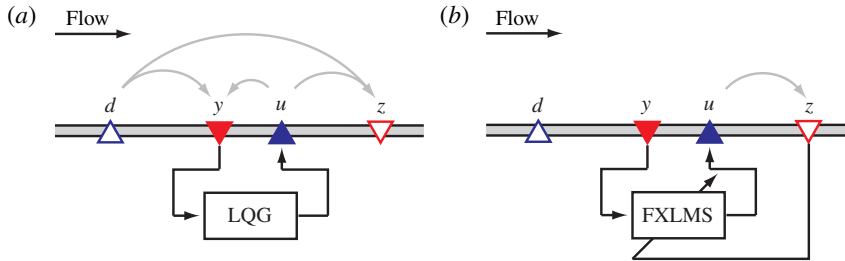$$u(n) = \sum_{i=1}^{N_k} K(i)\, y(n-i), \qquad (3.1)$$

FIGURE 3. Compensator schemes for static (LQG) (*a*) and adaptive (FXLMS) (*b*) strategies. The measurements by the error sensor *z* are used by the FXLMS algorithm to adapt to the current flow conditions. The grey lines indicate the input–output relations required to be modelled by each strategy.

where $u(n) = u(n\,\Delta t)$ and $y(n) = y(n\,\Delta t)$ are the time-discrete representations of the time-continuous signals $u(t)$ and $y(t)$, and $\Delta t = 1$ ms is the sampling time. The N_K coefficients $K(i)$ are the kernels of the filter and they describe how the compensator filters the measurements $y(n)$ in order to provide the control action $u(n)$.

One may identify two types of compensator, depending on whether the kernel is static or adaptive. In this work, the LQG regulator is chosen as representative of the static compensator class (figure 3*a*). It is designed by solving two independent optimization problems based on a state-space model of the plant (Glad & Ljung 2000). The estimation problem constructs a low-dimensional approximation of the flow from the measurements $y(t)$. The optimal control problem computes the signal $u(t)$ from the estimated state. An FXLMS algorithm represents the class of adaptive compensators (Sturzebecher & Nitsche 2003; Engert *et al.* 2008). As reported in figure 3(*b*), it uses the measurement signal of the error sensor $z(t)$ to dynamically adapt and is therefore able to adjust to varying conditions (such as Reynolds number) of the flow. The design requires a model of the input–output relation between the plasma actuator and the error sensor ($u \to z$). Compared with the LQG algorithm, FXLMS is only sub-optimal; we refer to Fabbiane *et al.* (2014) for more detailed information on both approaches.

Figure 4 compares the performance of the two compensators when the disturbance source is fed with a white-noise signal $d(t)$ for a wind-tunnel speed $U_{WT} = 12$ m s^{-1}. The flow filters the introduced disturbances and amplifies only a band of frequencies (Schmid & Henningson 2001); the spectrum of $z(t)$ that results from this process is depicted by the solid line. It should be noted that $z(t)$ is a measure of the wall-stress fluctuations and is therefore related to the amplitude of the TS wavepackets that are generated by the disturbance $d(t)$. The dashed and dot-dashed lines depict the spectrum $z(t)$ when the LQG and FXLMS compensators are applied: the FXLMS algorithm appears to be more effective than the LQG regulator. As mentioned in §2.1, the plasma actuator is operated at a mean high voltage $V = 7$ kV$_{pp}$, corresponding to an average specific-power consumption of $P = 16$ W m^{-1}. The resulting constant forcing is small and has therefore only a marginal stabilizing effect on the flow, as is shown by the dotted line in figure 4.

4. A DNS model of the flow

In order to provide a model for the LQG design, numerical simulations are used to simulate the flow in the test section. The experimental set-up described in §2
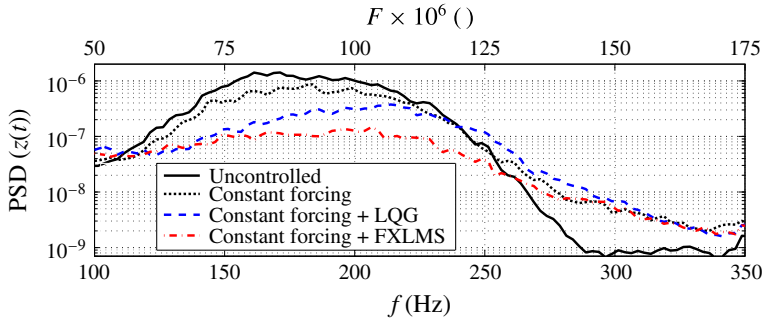
FIGURE 4. Experimental time-averaged power spectral density (PSD) functions for $z(t)$. The flow is excited by a white-noise signal $d(t)$. The top axis reports the non-dimensional frequency $F = (2\pi\nu/U_\infty^2)f$. The Reynolds number at the error sensor location is $Re_{x,z} = 375 \times 10^3$.

produces sufficiently small perturbations in order to not trigger nonlinear phenomena. Therefore, the linearized Navier–Stokes (NS) equations around a laminar zero-pressure-gradient boundary-layer flow are considered to describe the temporal evolution of the disturbances. The free-stream velocity $U_\infty = 14$ m s^{-1} and the displacement thickness in the beginning of the domain $\delta_0^* = 0.748$ mm are identified by a parameter fitting procedure of the laminar solution over 10 measured mean-velocity profiles between $x = 0$ mm and $x = 330$ mm. The resulting Reynolds number is $Re = U_\infty \delta_0^*/\nu = 656$, where ν is the kinematic viscosity. A pseudo-spectral DNS code is used to perform the simulations (Chevalier *et al.* 2007). Fourier expansion over $N_x = 768$ modes is used to approximate the solution along the streamwise direction, while Chebyshev expansion is used in the wall-normal direction on $N_y = 101$ Gauss–Lobatto collocation points. The computational domain is shown in figure 1.

The disturbance source and the plasma actuator are modelled by volume forcings. Each forcing term is decomposed into a constant spatial shape and a time-dependent part (i.e. the input signal). The forcing shape for the disturbance source is a synthetic vortex localized at the disturbance source position (Bagheri *et al.* 2009). The plasma actuator shape, instead, is modelled by a distributed streamwise forcing, according to the results by Kriegseis *et al.* (2013). As the forcing shape depends on the high-voltage supply to the actuator, a linearization around $V = 7$ kV$_{pp}$ is considered. The surface hot-wire sensors $y(t)$ and $z(t)$ are modelled as pointwise measurements of the skin-friction fluctuations.

Numerical simulations and experimental measurements of the performance of the LQG compensator are reported in figure 5. The flow is excited by a single-frequency constant-amplitude signal $d(t)$ with frequency $f_d = 200$ Hz. The amplitude of the velocity fluctuation in the flow is measured by a hot-wire probe mounted on a traverse system. A non-dimensional measure for the TS wave amplitude is introduced:

$$A_{TS,int}(x) = \frac{1}{\delta_0^*} \int_0^\infty \frac{|\mathcal{U}(x,y,f_d)|}{U_\infty} \mathrm{d}y = \frac{1}{\delta_0^*} \int_0^\infty A_{TS}(x,y) \mathrm{d}y, \qquad (4.1)$$

where $\mathcal{U}(x, y, f)$ is the Fourier transform of the streamwise component of the velocity. From figure 5(*a*) it can be observed that the direct simulation (black solid line) of the flow matches the experimental data (black circles) very well. When the LQG controller is active in experiments (blue squares), one order-of-magnitude
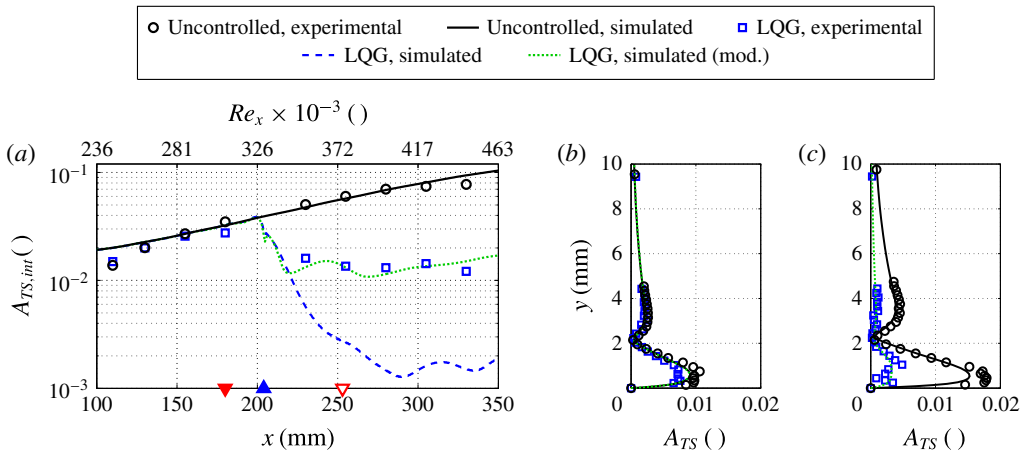
767 R1-6

FIGURE 5. The TS wave amplitude for $f_d = 200$ Hz. Lines and circles depict simulated and experimental data respectively. (*a*) The integral TS wave amplitude ($A_{TS,int}$) as a function of the streamwise position. The top axis reports $Re_x = ((x - x_{LE}) U_\infty)/\nu$, where x_{LE} is the leading-edge position. (*b*,*c*) The TS wave shape at two different x positions upstream and downstream of the actuator: (*b*) $x = 180$ mm; (*c*) $x = 253$ mm. The triangles indicate where the reference sensor, plasma actuator and error sensor are positioned, cf. figure 1.

reduction of disturbance amplitude is observed. This is, to the best of the authors' knowledge, the first time a computation-based LQG controller, designed without any fitting parameters or system identification, has suppressed disturbances in wind-tunnel experiments. However, the LQG controller is optimal for the exact model only, which it was designed for; as shown in figure 5(*a*), the attainable reduction of disturbance is two orders of magnitude when the controller is applied to the numerical simulation (dashed blue line). The difference of one order of magnitude is due to the fact that in experiments a steady forcing was applied in addition to the LQG control signal (see § 2). The performance prediction is improved if the average constant forcing by the plasma actuator is considered when computing the baseflow used for testing the compensator (green dotted line). This shows that there is a small difference between the modelled flow and the experimental flow.

In figure 5(*b*–*c*) the profile of the TS disturbance is compared with and without the controller active. The profiles are measured at the streamwise location of the reference sensor y and the error sensor z. From figure 5(*c*), one observes that the disturbance is damped all along the wall-normal direction, both in simulation (green dotted line) and in experiment (blue squares). A double-peaked shape is visible near the wall that can be explained by the proximity to the plasma actuator. In fact, the lower peak of the TS amplitude is located at the wall-normal position where Kriegseis *et al.* (2013) measured the maximum forcing of a similar plasma actuator. However, as the controlled TS wave evolves further downstream the double-peaked structure is less pronounced.

From figure 5(*b*,*c*) it can be seen that the maximum amplitude of the disturbance goes from $0.01 U_\infty$ at the y sensor location to $0.02 U_\infty$ at the z sensor location. These small amplitudes confirm the small-perturbation hypothesis, which the linear model and control are based on. In order to cancel the disturbance, the plasma actuator
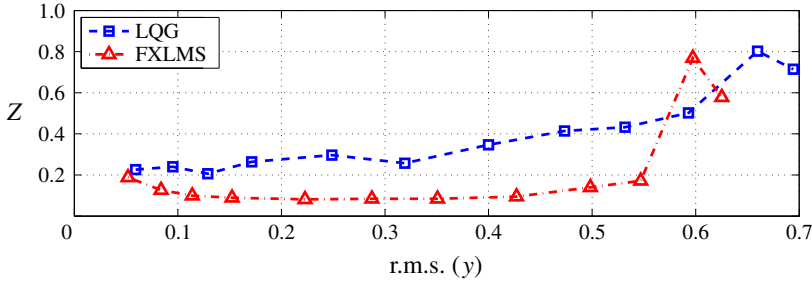
FIGURE 6. Effect of the TS wave amplitude on the performance indicator Z. The flow is excited by the disturbance source operated with a 200 Hz single-frequency signal.

induces velocity fluctuations of the same order of magnitude as the TS disturbance, i.e. between ± 0.14 and ± 0.28 m s^{-1}.

5. Robustness

In this section, the robustness of the two control techniques is analysed. In the present context, robustness refers to the capacity of the compensator to overcome differences between design and working conditions. In particular, the effect of deviations of the disturbance amplitude and the free-stream velocity on the control performance is investigated. It has been shown by Belson *et al.* (2013) and Fabbiane *et al.* (2014) that the current sensor/actuator configuration results in a feedforward control, which is well known to have robustness issues. The type of robustness analysis performed here is *ad hoc* in the sense that model uncertainties have been introduced systematically in order to assess the performance.

A 200 Hz single-frequency disturbance is used to investigate the robustness of the LQG controller against higher TS wave amplitude. The amplitude is gradually increased and the r.m.s. of the reference sensor signal $y(t)$ is used as an indicator of disturbance amplitude. A performance index is defined as the ratio between the r.m.s. of the controlled and uncontrolled sensor signals, i.e.

$$Z = \frac{\text{r.m.s.}(z_{ctr}(t))}{\text{r.m.s.}(z_{unctr}(t))}. \tag{5.1}$$

In figure 6, it can be observed that the controller performance is gradually degraded when the amplitude rises and is saturated at approximately r.m.s.$(y) = 0.6$. The FXLMS compensator, instead, is able to maintain good performance until an abrupt breakdown of the performance around r.m.s.$(y) = 0.6$. At these large amplitudes, the compensator adaptivity cannot compensate the strong nonlinearities of the flow.

Variation of the free-stream conditions may also degrade the control performance, since it changes the baseflow. The wind-tunnel speed is varied around the design condition $U_{WT} = 12$ m s^{-1}, changing the Reynolds number and, as a consequence, the stability properties of the flow (Schmid & Henningson 2001). A white noise is low-pass filtered with a cutoff frequency of 4 kHz and considered as a disturbance signal $d(t)$. The disturbance is monitored in order to ensure a 2D wavefront. The ratio between r.m.s.(y) and the wind-tunnel speed U_{WT} is kept constant and equal to 6.5×10^{-3} in order to avoid nonlinear effects. It should be noted that the asymptotic
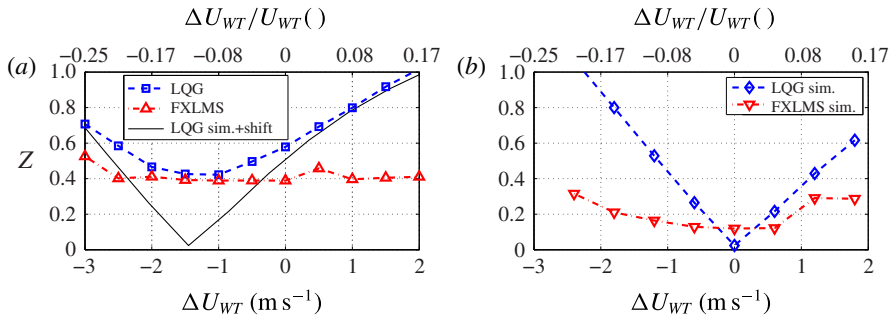
FIGURE 7. Effect of wind-tunnel speed variation ΔU_{WT} on the performance indicator Z. The solid line in (*b*) depicts the DNS data shifted to fit the experimental curve. The flow is excited by the disturbance source operated with a white-noise signal $d(t)$.

velocity U_∞ differs from U_{WT} because of blockage effects due to the presence of the flat plate and experimental equipment.

Figure 7(*a*) shows Z as a function of the wind-tunnel speed variation ΔU_{WT}. It is observed (blue dashed line) that the LQG performance is sensitive to variation of the free-stream velocity. One can note that the best performance is obtained for a velocity lower than the design speed. This shift can be attributed to the fact that an experimental flow can only be modelled numerically up to a certain accuracy. Uncertainties such as, for example, fluctuations in temperature (and thus a shift in Reynolds number) are unavoidable and lead to loss of performance, as described in the § 4. The FXLMS compensator, on the other hand, is able to adapt to the changed conditions. Even if the required input–output relation $u \to z$ – which is a static part of the FXLMS algorithm – is changed by the speed variation, the adaptive nature of the controller is able to compensate for this error and provide an almost unaltered performance for significant wind-tunnel speed variations.

The robust property of FXLMS is also confirmed by the numerical experiments (figure 7*a*). Similarly to the experiment, the free-stream velocity is varied with respect to its nominal value and the performance of the control action is monitored. At the design conditions $\Delta U_{WT} = 0$ m s^{-1}, the model for which the LQG was designed is a very accurate representation of disturbance behaviour. Interestingly, the attenuation achieved by the FXLMS algorithm is very close to the optimal performance of the LQG regulator. For the latter compensator however, Z increases linearly with ΔU_{WT}. This can be explained as follows. Assume that $z(t)$ is the superposition of the two counter-phase TS waves, one generated by the disturbance source and one by the plasma actuator,

$$z(t) = z_d(t) + z_u(t) = a \sin(\omega(t + \Delta \tau)) - a \sin(\omega t). \tag{5.2}$$

The leading-order effect of a change in the free stream is on the phase speed of the TS wave, which in turn results in a modification of the phase-shift parameter $\Delta \tau$. On rewriting expression (5.2) to highlight the role of $\Delta \tau$,

$$z(t) = 2a \sin\left(\omega \frac{\Delta \tau}{2}\right) \cos\left(\omega \left(t - \frac{\Delta \tau}{2}\right)\right) \approx a \omega \Delta \tau \cos\left(\omega \left(t - \frac{\Delta \tau}{2}\right)\right), \tag{5.3}$$

it is observed that for small values of $\omega \Delta \tau$, the amplitude of $z(t)$ is a linear function $\Delta \tau$. The black solid line in figure 7(*a*) shows the simulated LQG performance
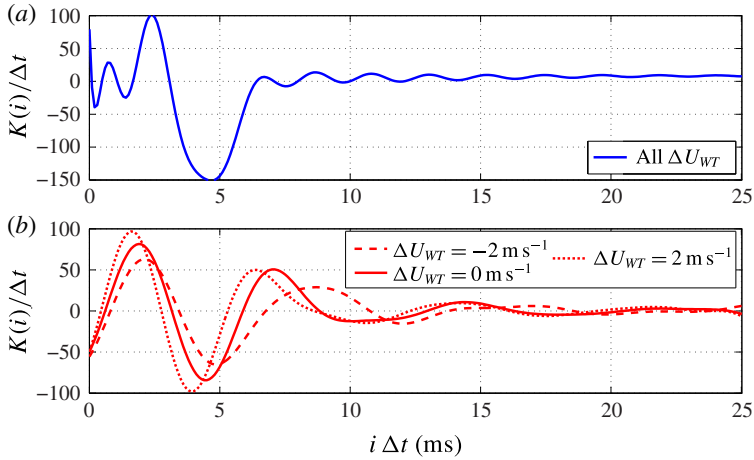
FIGURE 8. Compensator kernels $K(i)$ for different wind-tunnel speeds for LQG (*a*) and FXLMS (*b*). The solid line represents the design condition. When U_{WT} decreases (dashed line) or increases (dotted line), the FXLMS compensator adapts to the new conditions by stretching or shrinking the compensator kernel.

(dashed blue in figure 7*b*) when it is shifted to the left to coincide with minima of experimental control values of Z. It should be noted that Z corresponding to numerical data asymptotically approaches the experimental data (blue dashed line), showing the same linear behaviour as predicted by (5.3).

The solid lines in figure 8 depict LQG and FXLMS kernels for the design condition, i.e. $\Delta U_{WT} = 0$ m s^{-1}. When the wind-tunnel speed is decreased, the amplification of the TS wave is reduced and the propagation speed of the TS wave decreases, i.e. the TS wave moves slower than under design conditions. In this particular new condition, the FXLMS algorithm reacts by stretching the convolution kernel in time and reducing the magnitude of the $K(i)$ coefficients (dashed line in figure 8*b*). On the other hand, if the speed increases, the effect on the flow is opposite; the TS wave moves faster and is more amplified. Hence, the compensator reacts by shrinking the kernel and increasing the magnitude of the $K(i)$ coefficients (dotted line). The LQG kernel, instead, is fixed and does not adapt to the actual flow conditions.

To quantify the phase shift in the kernel, let τ represent the time for which the kernel attains its minimum value. Further, one may define the difference between the phase shifts of the two compensator kernels by $|\Delta\tau| = |\tau_{LQG} - \tau_{FXLMS}|$. In figure 9, a strong correlation between $|\Delta\tau|$ and the performance loss ΔZ (i.e. the gap between the two curves in figure 7*a*) is observed. This correlation shows that the compensator performance is depends mainly on a correct prediction of the time it takes for the TS wave to propagate from the reference sensor and to the plasma actuator. In the LQG approach, this information is given by the designed static model: any inaccuracy in this model may lead to an incorrect computation of the phase shift and, eventually, to a performance loss.

The FXLMS adaptive algorithm is not equivalent to a feedback sensor/actuator configuration (Belson *et al.* 2013). The FXLMS algorithm is able to adapt to modified flow conditions (i.e. weak nonlinearities, free-stream variation, etc.) by adapting its response (e.g. by stretching/shrinking the kernel when velocity fluctuations occur). However, it has to be noted that (i) the measurement signal $z(t)$ does not have a
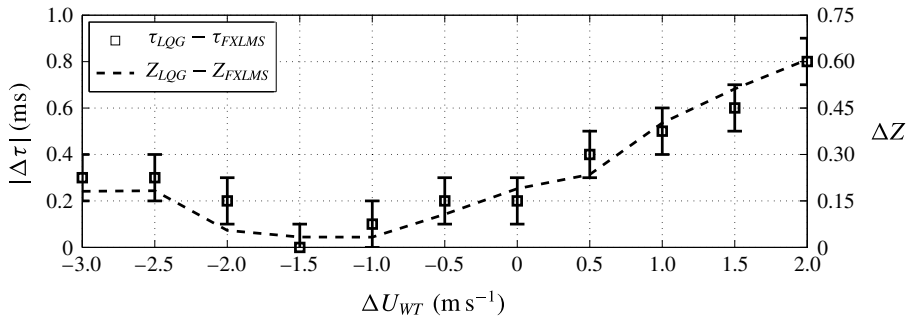
FIGURE 9. Correlation between the phase error $|\Delta\tau|$ (squares) and the performance loss ΔZ (dashed line) when the wind-tunnel speed is changed. The error bars report an interval $\pm\Delta t$ around each $\Delta\tau(U_{WT})$ point.

direct influence on the control signal but only on the kernel and (ii) the adaptation time scale – approximately 15 s from zero initial condition to the asymptotic value – is significantly larger than the TS wave time scale. Therefore, the compensator is able to adapt only to slow changes in the flow, and the adaptation loop cannot be characterized as a conventional feedback. These results extend and confirm our earlier work on the Kuramoto–Sivashinsky equation to a physical fluid flow (Fabbiane *et al.* 2014).

6. Conclusions

From a general viewpoint, the role of optimality has been overemphasized in investigations with linear theoretical approaches to transition and turbulence control. Although these studies provide important physical insight into performance limitations as well as the best achievable flow control performance, they remain at a proof-of-concept level, since any deviation of the design conditions can destabilize the controller; at best it will render the control performance sub-optimal. In this paper, it is shown that adaptivity plays a crucial role in achieving robustness in transition control, even when a simple 2D disturbance case is considered. While the optimal LQG outperforms simple wave-cancellation techniques significantly (Fabbiane *et al.* 2014), FXLMS obtains nearly as good performance as LQG but in addition possesses robustness, making it the choice for transition control.

References

ASTRÖM, K. J. & WITTENMARK, B. 1995 *Adaptive Control*, 2nd edn. Addison-Wesley.
BAGHERI, S., BRANDT, L. & HENNINGSON, D. S. 2009 Input–output analysis, model reduction and control of the flat-plate boundary layer. *J. Fluid Mech.* **620** (1), 263–298.
BAGHERI, S. & HENNINGSON, D. S. 2011 Transition delay using control theory. *Phil. Trans. R. Soc. Lond.* A **369**, 1365–1381.

BARBAGALLO, A., SIPP, D. & SCHMID, P. J. 2009 Closed-loop control of an open cavity flow using reduced order models. *J. Fluid Mech.* **641**, 1–50.

BARCKMANN, K. 2014, Active vortex generation using dielectric barrier discharge plasma actuators in laminar boundary layers. PhD thesis, Technischen Universitadt Darmstadt.

BELSON, B. A., SEMERARO, O., ROWLEY, C. W. & HENNINGSON, D. S. 2013 Feedback control of instabilities in the two-dimensional Blasius boundary layer: the role of sensors and actuators. *Phys. Fluids* **25**, 054106.

BEWLEY, T. R. & LIU, S. 1998 Optimal and robust control and estimation of linear paths to transition. *J. Fluid Mech.* **365**, 305–349.

BORODULIN, V. I., KACHANOV, Y. S. & KOPTSEV, D. B. 2002 Experimental study of resonant interactions of instability waves in self-similar boundary layer with an adverse pressure gradient: ii. Detuned resonances*. *J. Turbul.* **3**, 62.

CHEVALIER, M., SCHLATTER, P., LUNDBLADH, A. & HENNINGSON, D. S. 2007, A pseudo-spectral solver for incompressible boundary layer flows. *Tech. Rep.* TRITA-MEK 2007:07. KTH Mechanics, Stockholm, Sweden.

DOYLE, J. C. 1978 Guaranteed margins for LQG regulators. *IEEE Trans. Autom. Control* **23** (4), 756–757.

ENGERT, M., PÄTZOLD, A., BECKER, R. & NITSCHE, W. 2008 Active cancellation of Tollmien–Schlichting instabilities in compressible flows using closed-loop control. In *IUTAM Symposium on Flow Control and MEMS*, vol. 7, pp. 319–331. Springer.

FABBIANE, N., SEMERARO, O., BAGHERI, S. & HENNINGSON, D. S. 2014 Adaptive and model-based control theory applied to convectively unstable flows. *Appl. Mech. Rev.* **66** (6), 060801.

GLAD, T. & LJUNG, L. 2000 *Control Theory*. Taylor & Francis.

GOLDIN, N., KING, R., PÄTZOLD, A., NITSCHE, W., HALLER, D. & WOIAS, P. 2013 Laminar flow control with distributed surface actuation: damping Tollmien–Schlichting waves with active surface displacement. *Exp. Fluids* **54** (3), 1–11.

HAYKIN, S. 1986 *Adaptive Filter Theory*. Prentice-Hall.

JUILLET, F., MCKEON, B. J. & SCHMID, P. J. 2014 Experimental control of natural perturbations in channel flow. *J. Fluid Mech.* **752**, 296–309.

KRIEGSEIS, J., SCHWARZ, C., TROPEA, C. & GRUNDMANN, S. 2013 Velocity-information-based force-term estimation of dielectric-barrier discharge plasma actuators. *J. Phys. D* **46** (5), 055202.

KURZ, A., GOLDIN, N., KING, R., TROPEA, C. D. & GRUNDMANN, S. 2013 Hybrid transition control approach for plasma actuators. *Exp. Fluids* **54** (11), 1–4.

LUNDELL, F. 2007 Reactive control of transition induced by free-stream turbulence: an experimental demonstration. *J. Fluid Mech.* **585**, 41–71.

NORDSTRÖM, J., NORDIN, N. & HENNINGSON, D. 1999 The fringe region technique and the Fourier method used in the direct numerical simulation of spatially evolving viscous flows. *SIAM J. Sci. Comp.* **20** (4), 1365–1393.

SARIC, W. S., REED, H. L. & KERSCHEN, E. J. 2002 Boundary-layer receptivity to freestream disturbances. *Annu. Rev. Fluid Mech.* **34** (1), 291–319.

SCHMID, P. J. & HENNINGSON, D. S. 2001 *Stability and Transition in Shear Flows*, Applied Mathematical Sciences, vol. 142. Springer.

SEMERARO, O., BAGHERI, S., BRANDT, L. & HENNINGSON, D. S. 2013*a* Transition delay in a boundary layer flow using active control. *J. Fluid Mech.* **731** (9), 288–311.

SEMERARO, O., PRALITS, J. O., ROWLEY, C. W. & HENNINGSON, D. S. 2013*b* Riccati-less approach for optimal control and estimation: an application to two-dimensional boundary layers. *J. Fluid Mech.* **731**, 394–417.

STURZEBECHER, D. & NITSCHE, W. 2003 Active cancellation of Tollmien–Schlichting instabilities on a wing using multi-channel sensor actuator systems. *Intl J. Heat Fluid Flow* **24**, 572–583.

WÜRZ, W., SARTORIUS, D., KLOKER, M., BORODULIN, V. I., KACHANOV, Y. S. & SMORODSKY, B. V. 2012 Nonlinear instabilities of a non-self-similar boundary layer on an airfoil: experiments, DNS, and theory. *Eur. J. Mech.* B **31**, 102–128.